nature communications

Article

https://doi.org/10.1038/s41467-025-56621-3

Highly sensitive, responsive, and selective iodine gas sensor fabricated using AgI-functionalized graphene

Received: 9 May 2024

Accepted: 20 January 2025

Published online: 30 January 2025

Check for updates

Zhuo Chen[1,2,14], Qiong Lei[3,14], Yinchang Ma[1,14], Jinrong Wang[1], Yuan Yan[4], Jun Yin[5], Jiaqiang Li[1], Jie Shen[6], Guanxing Li[1], Tingting Pan[1], Xinglong Dong[7], Bambar Davaasuren[8], Yaping Zhang[8], Jefferson Zhe Liu[4], Jun Tao[9] ✉ & Yu Han[10,11,12,13] ✉

Radioactive molecular iodine (I_2) is a critical volatile pollutant generated in nuclear energy applications, necessitating sensors that rapidly and selectively detect low concentrations of I_2 vapor to protect human health and the environment. In this study, we design and prepare a three-component sensing material comprising reduced graphene oxide (rGO) as the substrate, silver iodide (AgI) particles as active sites, and polystyrene sulfonate as an additive. The AgI particles enable reversible adsorption and conversion of I_2 molecules into polyiodides, inducing substantial charge density variation in rGO. This mechanism facilitates exceptional sensitivity and selectivity, ultrafast response and recovery times, and room-temperature operation. A multifunctional sensor prototype fabricated utilizing this material achieves the fastest reported response/recovery times (22/22 seconds in dynamic mode and 4.2/11 seconds in static mode) and a detection limit of 25 ppb, surpassing standards set by the Occupational Safety and Health Administration (OSHA) and the National Institute for Occupational Safety and Health (NIOSH), while outperforming commercial I_2 gas sensors. This work provides profound insights into the design of I_2 sensing materials and mechanisms for real-world applications.

Nuclear energy, recognized as a clean and sustainable energy source, is crucial in addressing the global energy predicament[1]. However, the operation of nuclear reactors raises safety concerns, including the generation of volatile radioactive substances[2,3]. Among them, iodine isotopes, specifically ^{129}I and ^{131}I, in their gaseous molecular form (I_2)[4,5], are major hazards that seriously endanger human health and the environment[5–7]. Current iodine detection methods at nuclear plants and environmental monitoring stations are cumbersome, generally

[1]Physical Sciences and Engineering Division, King Abdullah University of Science and Technology (KAUST), Thuwal, Saudi Arabia. [2]Hebei Onlysense Technology Co. Ltd, Tangshan, China. [3]Macao Institute of Materials Science and Engineering (MIMSE), Faculty of Innovation Engineering, Macau University of Science and Technology, Taipa, Macao, China. [4]Department of Mechanical Engineering, The University of Melbourne, Parkville, VIC, Australia. [5]Department of Applied Physics, The Hong Kong Polytechnic University, Kowloon, Hong Kong, China. [6]School of Materials Science and Engineering, Nanyang Technological University, Singapore, Singapore. [7]Catalyst Center of Excellence (CCoE), Research and Development Center, Saudi Aramco, Dhahran, Saudi Arabia. [8]Imaging and Characterization Core Lab, KAUST, Thuwal, Saudi Arabia. [9]Department of Neurosurgery, First Affiliated Hospital of China Medical University, Shenyang, China. [10]School of Emergent Soft Matter, South China University of Technology, Guangzhou, China. [11]Center for Electron Microscopy, South China University of Technology, Guangzhou, China. [12]Guangdong Basic Research Center of Excellence for Energy & Information Polymer Materials, Guangzhou, China. [13]State Key Laboratory of Pulp and Paper Engineering, South China University of Technology, Guangzhou, China. [14]These authors contributed equally: Zhuo Chen, Qiong Lei, Yinchang Ma ✉e-mail: jtao@cmu.edu.cn; hanyu@scut.edu.cn

not conducted in real-time, and necessitate bulky equipment[8–10]. Hence, developing portable iodine gas sensors, capable of quickly identifying I_2 at low concentrations, is crucial for safeguarding human health, securing nuclear facilities, and preserving the environment.

An ideal gas sensing material should exhibit specific adsorption towards the target gas and a unique signal amplification mechanism to ensure high selectivity and sensitivity, respectively. Fast and reversible sorption of the target gas is also crucial for achieving a swift response and recovery during the sensor's operation. Various sensing materials and mechanisms have been explored for developing iodine gas sensors[11–19]. Polymeric materials, featuring excellent processability, have been utilized to detect I_2 through changes in conductivity or fluorescence. However, conductive polymers typically exhibit limited sensitivity, with detection thresholds at the parts per million (ppm) level[11,12], and fluorescent polymers, despite their high sensitivity, face drawbacks of low detection accuracy and lack of reusability[13,14]. Nanoporous framework materials, such as metal-organic frameworks (MOFs) and covalent organic frameworks (COFs), can enhance the sensitivity and selectivity of sensors by specifically facilitating I_2 adsorption, but their constrained microporous structures impede the diffusion of I_2 molecules, resulting in long response and recovery times[15–17]. In addition, silver (Ag) particles are often incorporated into I_2 sensing materials to act as active centers, which react with I_2 to form silver iodide (AgI), thereby generating the sensing signals. However, since this reaction is irreversible, Ag-based I_2 sensors usually lack reusability, or they require high temperatures and prolonged periods to recover[18,19]. Currently, developing I_2 gas sensors that combine high sensitivity and selectivity with rapid response and recovery capabilities remains a significant challenge.

Graphene exhibits several desirable properties for gas sensing, such as a large surface area, high charge carrier mobility, and a zero bandgap. Theoretically, even a minimal quantity of adsorbed species on graphene can induce swift and substantial changes in its electronic properties, thereby producing significant sensing signals[20,21]. However, pristine graphene is found to be suboptimal for sensing applications, largely attributed to its low selectivity for specific molecules and its propensity to agglomerate due to $\pi-\pi$ interactions, resulting in a notable decrease in available surface area[22–24]. In practical use, graphene often undergoes surface modifications to enhance its dispersion without compromising its intrinsic electronic properties[25,26]. Reduced graphene oxide (rGO) is the most commonly used graphene alternative, favored for its properties akin to graphene and its availability on a large scale[27]. Despite the extensive research on sensors employing graphene or rGO, their application in I_2 sensing is still largely unexplored.

In this study, we fabricated an I_2 sensing material by functionalizing rGO with AgI particles, targeting simultaneous high sensitivity and selectivity, rapid response, and easy recovery. This composite material was designed based on three main considerations. Firstly, the presence of AgI on rGO can specifically enhance the adsorption of I_2, providing high sensing selectivity. Secondly, the interaction of AgI with I_2 facilitates the formation of polyiodides. These polyiodides can cause a more pronounced charge density change in rGO than I_2 alone, thus amplifying the electrical signal induced by I_2 adsorption. Thirdly, the AgI-mediated I_2 adsorption process is both quick and reversible, ensuring swift response and recovery with the introduction and removal of I_2. Consistent with our expectations, the fabricated sensing material exhibits high selectivity towards I_2 over various oxidizing/reducing gases and features an exceptionally low limit of detection (LoD) at the parts per billion (ppb) level. Remarkably, this performance can be achieved under both dynamic and static conditions, which are used to simulate detection in flowing gases and confined spaces, respectively. Moreover, the response and recovery times of this sensing material range from 4 to 22 s, significantly faster than traditional I_2 sensors, which usually take minutes or even hours to respond or recover. Using this composite material, we constructed a multifunctional I_2 sensor prototype and conducted tests under various simulated scenarios, comparing it with commercial I_2 sensors. The results of these tests indicate that, compared to commercial devices, our sensor exhibits a lower LoD, along with a response and recovery time that is several tens of times faster, showcasing its significant potential for real-world applications.

Results

Design and preparation of the sensing material

The adsorption of I_2 molecules on the surface of graphene (or rGO) causes changes in the charge density and band structure of the latter, thereby altering its electrical conductivity and generating electrical signals. This forms the basis for using graphene as a sensing material for I_2 detection. Density functional theory (DFT) calculations were conducted to validate this hypothesis (see Supplementary Section I for calculation methods). As shown in Fig. 1a, graphene exhibits its Fermi level situated at the Dirac point of the energy band. Upon I_2 adsorption, iodine atoms attract electrons from graphene through Coulombic forces, resulting in a reduction in graphene's charge density and a downward shift of its Fermi level away from the Dirac point (Fig. 1b). The corresponding diagrams of density of states are presented in Supplementary Fig. 2. Consequently, extra holes are created as free carriers in graphene, enhancing its conductivity, which can be probed electrically.

Therefore, the key to achieving a more significant sensing signal lies in inducing a greater variation in charge density of the sensing material in response to the target gas. Considering that polyiodide species, such as I_3^- and I_5^-, are commonly formed during the adsorption of I_2, especially when the adsorbent contains electron-rich groups[28–30], we investigate their influence on the electronic structure of graphene. The results reveal that I_3 and I_5 can induce more pronounced changes in the charge density and Fermi level of graphene than I_2, as illustrated in Fig. 1c, d. This insight suggests that functionalizing graphene to facilitate the formation of polyiodides could be a potent strategy to amplify electrical signals, thereby increasing the sensitivity of the sensor. Furthermore, it has been documented that incorporating AgI into the adsorbent can facilitate I_2 adsorption while inducing reversible conversion between I_2 and polyiodides[31,32].

Based on these theoretical and experimental insights, we have prepared a composite material, termed Ag-PSS-rGO, using a one-step assembly method (see Supplementary Section II for details). This material primarily consists of rGO with dispersed Ag particles and incorporates polystyrene sulfonate (PSS) to facilitate the dispersion of rGO during the material's preparation (Fig. 1e).

X-ray photoelectron spectroscopy (XPS) demonstrated the presence of PSS and Ag in the composite, as evidenced by the distinct *S 2p* peak at 168.4 eV, which is characteristic of sulfonic ($-SO_3^-$) groups, along with *Ag 3d* peaks at 373.9 eV and 367.9 eV (Supplementary Fig. 4a, b). X-ray diffraction (XRD) and atomic force microscopy analyses revealed that Ag nanocrystals, varying in size from a few nanometers to several tens of nanometers, are uniformly dispersed throughout the composite (Supplementary Fig. 4c, d). Scanning transmission electron microscopy combined with energy-dispersive X-ray spectroscopy (EDS) further confirmed uniform distributions of C, S, and O, as well as Ag particles, within the composite (Supplementary Fig. 5). These findings collectively indicate the effective integration of the three constituent elements within the composite material. Notably, the incorporation of PSS into the composite serves exclusively to improve its dispersion in solution—a vital aspect for sensor fabrication, and this does not impact the charge density of graphene (see Supplementary Section IV for further discussions).

The Ag-PSS-rGO composite material is deliberately exposed to I_2 vapor, which reacts with the Ag particles to form AgI particles. This

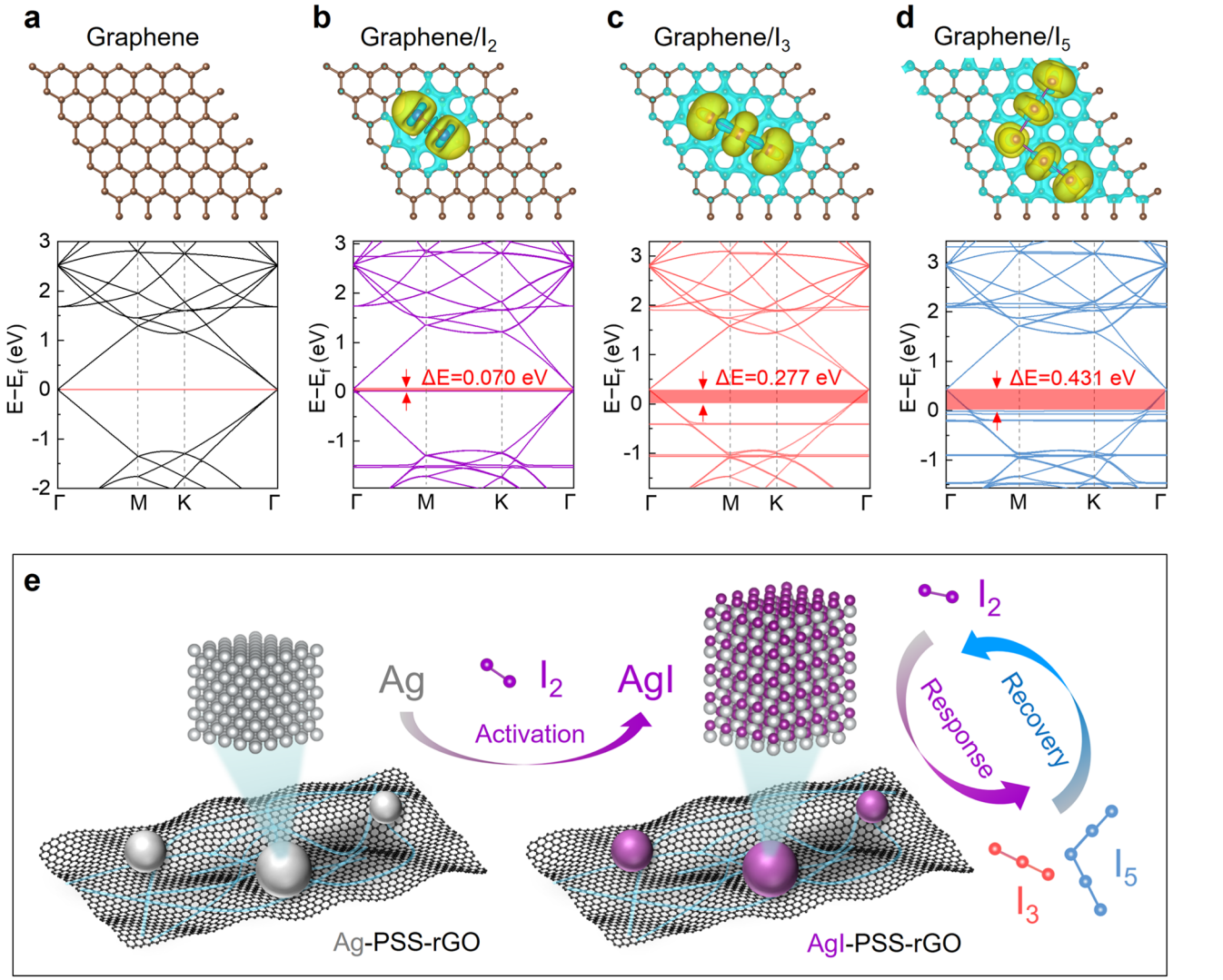

Fig. 1 | Design rationale for iodine gas sensing material. a Optimized atomic structure and band structure of graphene. Charge density difference plots and band structures of graphene/I_2 (**b**), graphene/I_3 (**c**), and graphene/I_5 (**d**) at the isosurface of 0.001 e per Bohr^3. Brown and purple spheres represent carbon and iodine atoms, respectively. Yellow regions indicate electron accumulation, while cyan regions stand for electron deficiency. **e** Schematic illustration of the activation, response and recovery processes of I_2 sensing on the designed composite material. Purple, red, and blue atoms are used to distinguish I_2, I_3, and I_5, respectively. Source data are provided as a Source Data file.

reaction serves as an activation process. The resulting AgI particles subsequently act as active sites for I_2 detection (Fig. 1e), as will be discussed in later sections.

Operando characterizations

An *operando* platform integrating XRD and Raman spectroscopy was used to monitor structural and compositional changes within the Ag-PSS-rGO sensing layer throughout the I_2 detection process (see Fig. 2a and Supplementary Fig. 7). Data was collected at a series of selected time points, distributed across different stages, including activation, response, and recovery (Fig. 2b).

During the activation stage, *operando* XRD data showed that upon first exposure to I_2 vapor, the Ag crystals in the Ag-PSS-rGO composite fully transformed into AgI (hexagonal β phase) (profiles ① and ② in Fig. 2c). Supplementary ex-situ transmission electron microscopy, selected area electron diffraction, and EDS analysis confirmed this transformation and further revealed that it was coupled with crystal agglomeration, resulting in the formation of AgI particles that are significantly larger than the original Ag particles[33,34] (Supplementary Figs. 8 and 9). In the *operando* Raman spectra, a band appeared at 112.2 cm^{-1} during the activation stage (profiles ① and ② in Fig. 2d), attributed to the E_2 vibrational mode of AgI[35] (Supplementary Fig. 10a). The emergence of this band signals the transformation of Ag to AgI, consistent with the *operando* XRD findings.

As the system transitions into the response stage, re-exposure to I_2 vapor results in no further phase transitions or transformations in the AgI composition, as indicated by the unchanged *operando* XRD pattern (profile ④ in Fig. 2c). Meanwhile, three distinct bands emerged in the *operando* Raman spectra at 81.3, 106.7, and 171.5 cm^{-1}. These bands, due to their intense strength, overshadow the AgI band, rendering it invisible in the spectrum (profile ③ in Fig. 2d). The bands at 106.7, and 171.5 cm^{-1} are generally recognized as stretching vibration modes of I_3^- and I_5^-, respectively[28]. While the specific assignment of the band at 81.3 cm^{-1} is currently unclear, it is likely related to interactions between iodide species and the surfaces of AgI crystals. Upon prolonged exposure to I_2 vapor, two new bands at 179.6 and 190.2 cm^{-1} emerged (profile ④ in Fig. 2d), corresponding to the A_g and B_{3g} vibration modes of molecular iodine, respectively[36] (Supplementary Fig. 10b). These observations indicate that the initially adsorbed iodine molecules are converted into polyiodides, and after this conversion

https://doi.org/10.1038/s41467-025-56621-3

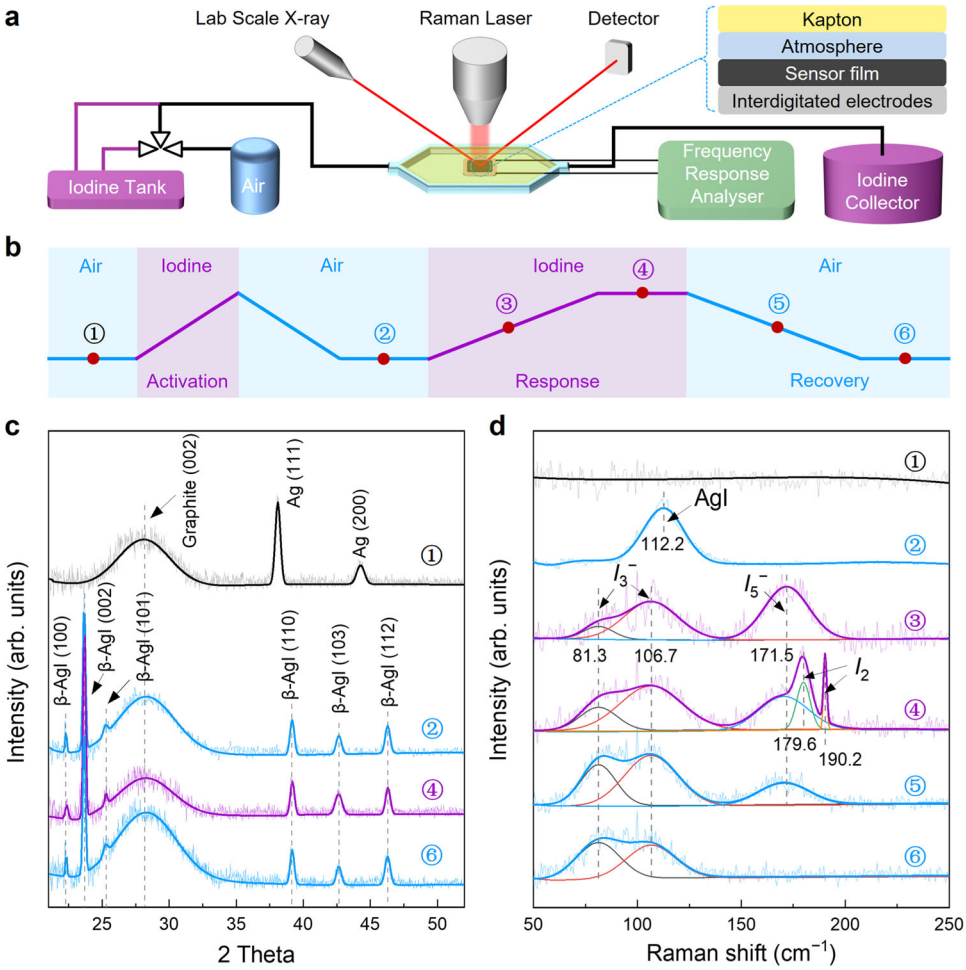

Fig. 2 | *Operando* characterizations for the iodine sensing process. a Schematic diagram of the *operando* Raman spectroscopy and XRD setup. **b** Diagram illustrating the various stages of the I_2 gas sensing process on the Ag-PSS-rGO composite. The numbers ①–⑥ indicate the points at which *operando* XRD and Raman data were collected. **c** *Operando* XRD profiles and **d** *Operando* Raman spectra, collected during the alternating exposure to I_2 vapor and air, corresponding to the stages marked in **b**. The total flow rate is 200 standard cubic centimeters per minute (sccm), and the concentration of I_2 vapor is 75 ppm. The light-colored, noisy curves represent the raw data, while the deep-colored, smooth curves correspond to the refined data obtained after fitting. Source data are provided as a Source Data file.

reaches saturation, subsequently adsorbed iodine molecules just accumulate.

Finally, during the recovery stage, when the gas flow containing I_2 vapor was switched back to pure air, the Raman bands characteristic of molecular I_2 vanished instantly, while those associated with I_3^-/I_5^- polyiodides gradually diminished in intensity (profiles ⑤ and ⑥ in Fig. 2d). This observation implies that I_2 molecules can be quickly desorbed from the composite, whereas the removal of polyiodides, presumably through their decomposition back into molecular I_2, takes place relatively slowly.

In our *operando* Raman experiments, the signal of I_3^- did not completely vanish during the recovery process, likely due to contamination in the experimental setup, specifically trace amounts of iodine deposited in the tubing that continued to be released and reacted with AgI. If we move the iodine-adsorbed sample to a new chamber with fresh tubing to conduct the "recovery" experiment, the signal of I_3^- would disappear completely (Supplementary Fig. 11), proving that the polyiodides can be fully desorbed. The phenomena observed in the *operando* Raman experiments, specifically the formation of polyiodide species followed by the accumulation of I_2 and their subsequent disappearance in the reverse order, show high reproducibility across successive response/recovery cycles (Supplementary Fig. 12). This consistency underscores the robustness and reliability of the designed composite as a sensing material. In contrast, when the same *operando* Raman experiment was performed on the composite without Ag inclusion, only weak Raman signals related to molecular iodine were observed, and no polyiodides were detected (Supplementary Fig. 13). This result highlights the vital role of AgI in promoting the adsorption of I_2 molecules and their conversion into polyiodides.

Iodine sensing performance

The Hall resistance of Ag-PSS-rGO increases as the magnetic field intensified, indicating its p-type semiconductor nature (Supplementary Fig. 14). Consequently, the adsorption of oxidative gases is expected to raise its hole concentration, thereby reducing its resistance. This forms the physical basis for its application in iodine sensors.

Iodine sensor modules were fabricated through the deposition of an aqueous dispersion of Ag-PSS-rGO onto interdigitated electrodes, followed by air drying (Supplementary Fig. 15). The current-voltage characteristics of the Ag-PSS-rGO sensor module exhibit excellent linearity within the range of −0.5 to 0.5 V (Supplementary Fig. 16), indicating negligible contact resistance and the absence of a Schottky barrier[27,37]. This ensures the accuracy of gas sensing measurements. The sensor module was then activated by exposing it to saturated I_2 vapor at room temperature for 1 min. The activated sensor module, referred to as AgI-PSS-rGO, was tested in both dynamic and static

https://doi.org/10.1038/s41467-025-56621-3

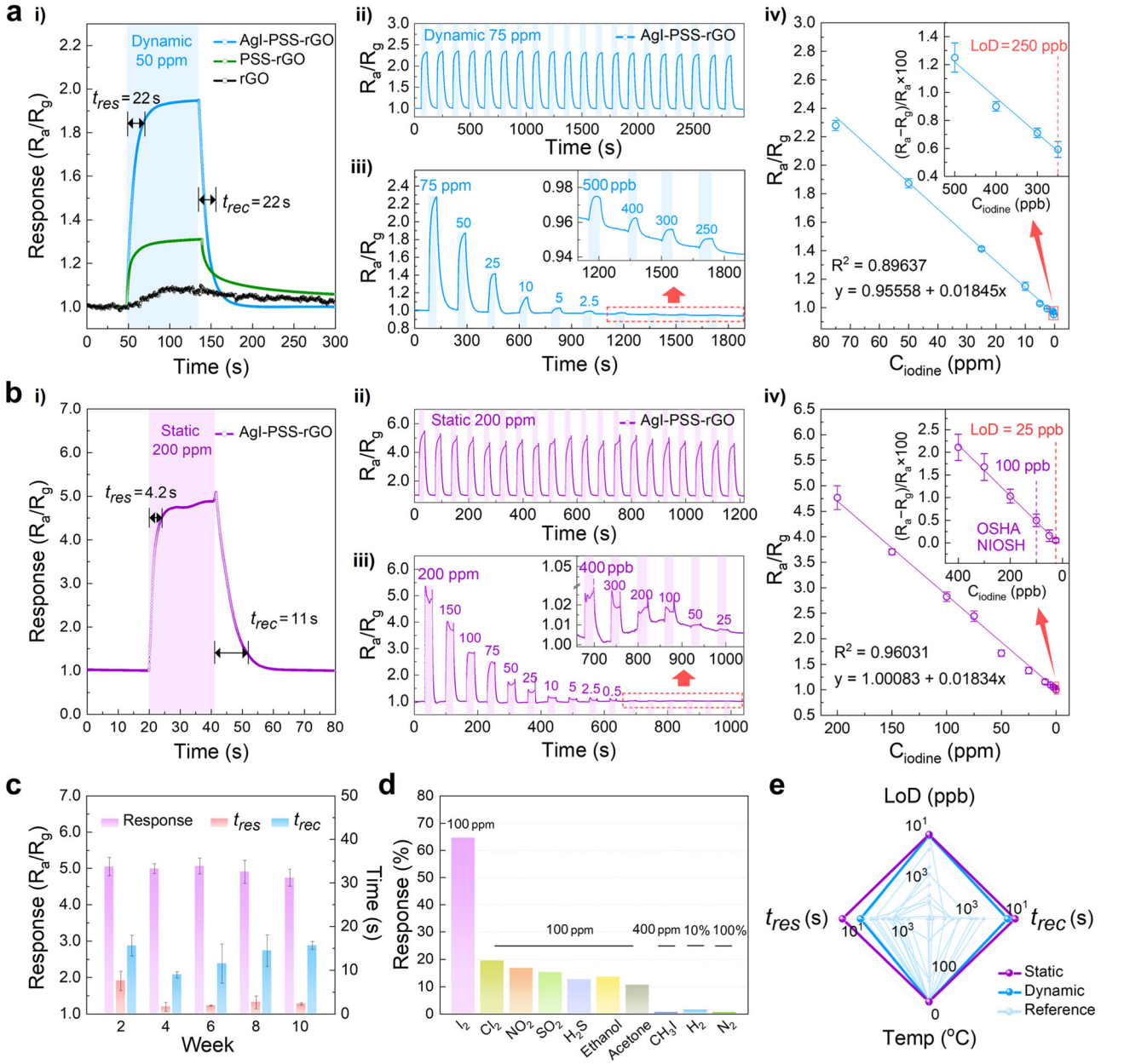

Fig. 3 | Performance evaluation of the AgI-PSS-rGO sensor module. a Dynamic I_2 gas sensing at room temperature: **i** Response-recovery profiles for AgI-PSS-rGO, PSS-rGO, and rGO sensor modules at 50 ppm I_2 gas. **ii** Consecutive 20-cycle response-recovery profile of AgI-PSS-rGO upon exposure to and removal from 75 ppm I_2 gas. **iii** Consecutive response-recovery profile of AgI-PSS-rGO with varying I_2 concentrations ranging from 75 ppm to 250 ppb. **iv** Corresponding plot of response values versus I_2 concentrations. **b** Static I_2 gas sensing at room temperature: **i** Response-recovery profile of AgI-PSS-rGO at a 200 ppm I_2 concentration. **ii** Consecutive 20-cycle response-recovery profile of AgI-PSS-rGO upon exposure to and removal from 200 ppm I_2 gas. **iii** Consecutive response-recovery profile of AgI-PSS-rGO with varying I_2 concentrations ranging from 200 ppm to 25 ppb. **iv** Corresponding plot of response values versus I_2 concentrations. **c** A ten-week aging test with biweekly inspections of AgI-PSS-rGO at a 200 ppm I_2 concentration. **d** Responses of AgI-PSS-rGO to I_2 and other interfering gases including Cl_2, NO_2, SO_2, H_2S, ethanol, acetone, CH_3I, H_2 and N_2. For ease of comparison, the sensing response is expressed as to $Response\ (\%) = (R_a - R_g)/R_a \times 100$ for oxidizing gases, and $Response\ (\%) = (R_g - R_a)/R_g \times 100$ for reducing gases. **e** Comparison of AgI-PSS-rGO with 16 previously reported I_2 gas sensors regarding limit of detection (LoD), operating temperature (Temp), response time (t_{res}), and recovery time (t_{rec}) (see Supplementary Table 1 for specifics). The error bars in **a**–**c** represent the standard deviations from five measurement cycles. Source data are provided as a Source Data file.

modes to mimic real-world scenarios for iodine detection in flowing gases and confined spaces, respectively. The sensing response value is defined as $Response = R_a/R_g$, where R_a and R_g represent the resistances measured in air and target gas, respectively.

In dynamic measurements, the AgI-PSS-rGO sensor module encountered continuous, alternating flows of I_2 vapor and air, controlled by a variable range dynamic gas distribution system (Supplementary Fig. 17). For comparison purposes, sensor modules fabricated using rGO and the PSS-rGO composite were tested under identical conditions. As depicted in Fig. 3a(i), upon exposure to 50 ppm iodine vapor, the sensor modules of rGO and PSS-rGO demonstrated response values of 1.09 and 1.31, respectively. The enhanced sensitivity of rGO related to the addition of hydrophilic PSS can be ascribed to PSS's capability to improve the dispersion of hydrophobic rGO, thus expanding the accessible sensing area of rGO. Incorporating Ag into the composite further boosts the sensor's sensitivity, with the degree of enhancement being dependent on the Ag content (Supplementary Fig. 18). Specifically, the AgI-PSS-rGO sensor module with an Ag

loading of 0.68 wt% achieves its maximum response value of 1.93 (Fig. 3a(i)). This substantial enhancement in sensitivity aligns with our strategic design, wherein AgI particles enhance the sensing signal by promoting I_2 adsorption and the generation of polyiodides. Additionally, the AgI-PSS-rGO sensor module exhibits an ultrafast response (response time, $t_{res} = 22$ s) and recovery (recovery time, $t_{rec} = 22$ s) (Fig. 3a(i)). These times represent the duration required to achieve 90% of the total resistance change upon exposure to I_2 and air, respectively[38]. This favorable performance suggests that the adsorption of I_2 molecules and their subsequent conversion into polyiodides are reversible processes with rapid kinetics.

Over 20 consecutive response/recovery cycles with 75 ppm of iodine vapor, the AgI-PSS-rGO sensor module displayed an average response value of 2.32 and a minimal standard deviation of 3.37%, indicating high performance stability (Fig. 3a(ii)). Furthermore, the AgI-PSS-rGO sensor module demonstrated a linear response to I_2 concentration over a broad range, from 75 ppm down to 250 ppb (Fig. 3a(iii–iv)). Limited by the gas distribution capacity of our experimental setup, the lowest measurable LoD was 250 ppb. However, given the sensor's minimal noise (Supplementary Fig. 19a) and its linear response to concentration changes (Supplementary Fig. 19b), we estimate the theoretical LoD could be as low as 27 ppb. This estimation is based on the principle of three times the signal-to-noise ratio[39]. The resistance behaviors of these sensor modules during dynamic measurements are shown in Supplementary Fig. 20.

In static measurements, the sensor module was exposed to a stable atmosphere, with the I_2 concentration regulated by a static gas distribution system (Supplementary Fig. 21). Upon exposure to 200 ppm iodine vapor, the AgI-PSS-rGO sensor module exhibited response and recovery times of 4.2 and 11 s, respectively (Fig. 3b(i)). This faster response, relative to that observed in dynamic mode, can be ascribed to two primary reasons. Firstly, the sorption of iodine molecules on AgI-PSS-rGO reaches equilibrium faster in static mode than in dynamic mode, owing to the absence of turbulence from the continuous gas flow. Secondly, the switching between I_2 vapor and air occurs instantaneously in static mode, whereas in dynamic mode, it requires some time to complete. When tested at a relatively high I_2 concentration of 200 ppm, the AgI-PSS-rGO sensor module showed stable performance and robust durability, exhibiting highly consistent response and recovery patterns across numerous consecutive cycles (Fig. 3b(ii)), and also during a ten-week test with biweekly evaluations (Fig. 3c).

Compared to the dynamic system, the static system allows for precise measurements across a wider I_2 concentration range from 200 ppm to 25 ppb. Within this spectrum, the AgI-PSS-rGO sensor module shows a strong linear correlation between response values and I_2 concentrations, demonstrating a reliable LoD of 25 ppb (Fig. 3b(iii–iv)). This LoD is significantly below the International Standards for iodine gas exposure (0.1 ppm, 1 mg/m^3) set by OSHA and NIOSH[40,41]. The resistance behavior of the AgI-PSS-rGO sensor module during static measurements is shown in Supplementary Fig. 22.

Notably, the AgI-PSS-rGO sensor module demonstrates a high selectivity for I_2. Its response to I_2 is over three times greater than to other strong oxidizing or reducing gases, such as Cl_2, NO_2, SO_2, and H_2S, when measured at identical concentrations (Fig. 3d). When tested in the presence of these interfering gases, the AgI-PSS-rGO sensor module maintained a reversible response to I_2 (Supplementary Fig. 23a–d). Its response moderately increased in the presence of Cl_2, NO_2, and SO_2, while it slightly decreased with H_2S (Supplementary Fig. 23e). Additionally, the sensor effectively distinguishes I_2 from typical volatile organic compounds (VOCs), such as ethanol and acetone, while exhibiting negligible response to CH_3I, H_2, and N_2, which are commonly present in nuclear plant off-gases (Fig. 3d). Conventional Ag-based sensors are expected to exhibit a noticeable response to CH_3I because Ag can interact with CH_3I through dissociative chemisorption. In contrast, our sensor material employs AgI as the active site, which effectively facilitates the adsorption of I_2 and its subsequent conversion to polyiodides. However, it does not exhibit a particular response to CH_3I, thereby demonstrating unique selectivity for I_2 over CH_3I.

Figure 3e presents a performance comparison between the AgI-PSS-rGO sensor and sixteen iodine gas sensors from earlier research. This analysis indicates that AgI-PSS-rGO is superior to these benchmarks in LoD, response time, and recovery time (see Supplementary Table 1 for specifics). Another notable advantage of AgI-PSS-rGO compared to many reported iodine gas sensors is its ability to operate at room temperature, eliminating the need for elevated operating temperatures. A comparison of selectivity was not conducted due to a lack of sufficient data in the literature.

The AgI-PSS-rGO sensor module maintains a stable response and recovery behavior toward 50 ppm I_2 across different temperatures (25 °C to 150 °C) and relative humidity levels (19% to 88%). The response (R_a/R_g) decreases monotonically with increasing temperature (Supplementary Fig. 24), while generally increasing with rising humidity, with a more pronounced effect at high relative humidities (>64%) (Supplementary Fig. 25).

Fabrication and evaluation of a sensor prototype

A multi-functional iodine gas sensor prototype was fabricated by integrating the AgI-PSS-rGO sensor module with various components through a printed circuit board design, as illustrated in Fig. 4a. The predetermined effects of temperature and humidity on the response values (Fig. 4b) have been integrated into the sensor's algorithm for calibration. Detailed descriptions of the device fabrication with circuit diagrams are provided in the Supplementary Section VII.

This compact prototype (15 cm*6.8 cm*3.1 cm, 320 g) is equipped with a TFT multi-touch screen that enables comprehensive and real-time feedbacks through an adaptable user interface. It displays critical metrics such as I_2 concentration, temperature, humidity, test duration, and dynamic I_2 sensing curves (Fig. 4b, Supplementary Movie 1). Additionally, the prototype facilitates wireless data transmission to PC terminals, with software that synchronously displays real-time variations in I_2 concentration, allowing for continuous and remote monitoring (Fig. 4b, Supplementary Movie 2).

The fabrication of this prototype enables a direct comparison with commercially available iodine sensors. For this comparison, two commercial sensors have been chosen: one operates on the electrochemical detection principle (Manufacturer: Gas Sensing; Model: D − 16 PortaSens III), and the other employs the PID detection principle (Manufacturer: Empaer; Model: APES − ZI2 − T10).

The three sensors were first assessed for real-time dynamic I_2 detection. Iodine vapor and air were alternately introduced to trigger the sensors' response and subsequent recovery. As illustrated in Supplementary Movie 3, our prototype demonstrated markedly faster response and recovery, despite both commercial devices being equipped with a pumping mode to enhance their response and recovery speed. Specifically, when exposed to 50 ppm I_2 vapor, our prototype exhibited a response time of 12 s. In comparison, the response times of the two commercial sensors were approximately 235 s and 620 s, respectively. Moreover, our prototype demonstrated a recovery time of 26 s, which is 63 and 84 times faster than the recovery times of the two commercial sensors, respectively (Fig. 4c). This highlights the superiority of the unique reversible sensing mechanism based on AgI-PSS-rGO. Furthermore, our prototype demonstrated accuracy and sensing linearity ($y = 0.06147 + 0.98501x$, $R^2 = 0.99958$) comparable to commercial sensors ($y = -0.18701 + 1.01858x$, $R^2 = 0.99937$ and $y = -0.21743 + 1.00784x$, $R^2 = 0.99862$) within the I_2 concentration range of 100 ppb–50 ppm. Notably, it succeeded in detecting I_2 concentrations below 100 ppb, whereas commercial devices failed (Fig. 4d).

The three sensors were subsequently tested for static I_2 detection in a confined space, using a 1 m^3 gas sensing chamber (Fig. 4e,

https://doi.org/10.1038/s41467-025-56621-3

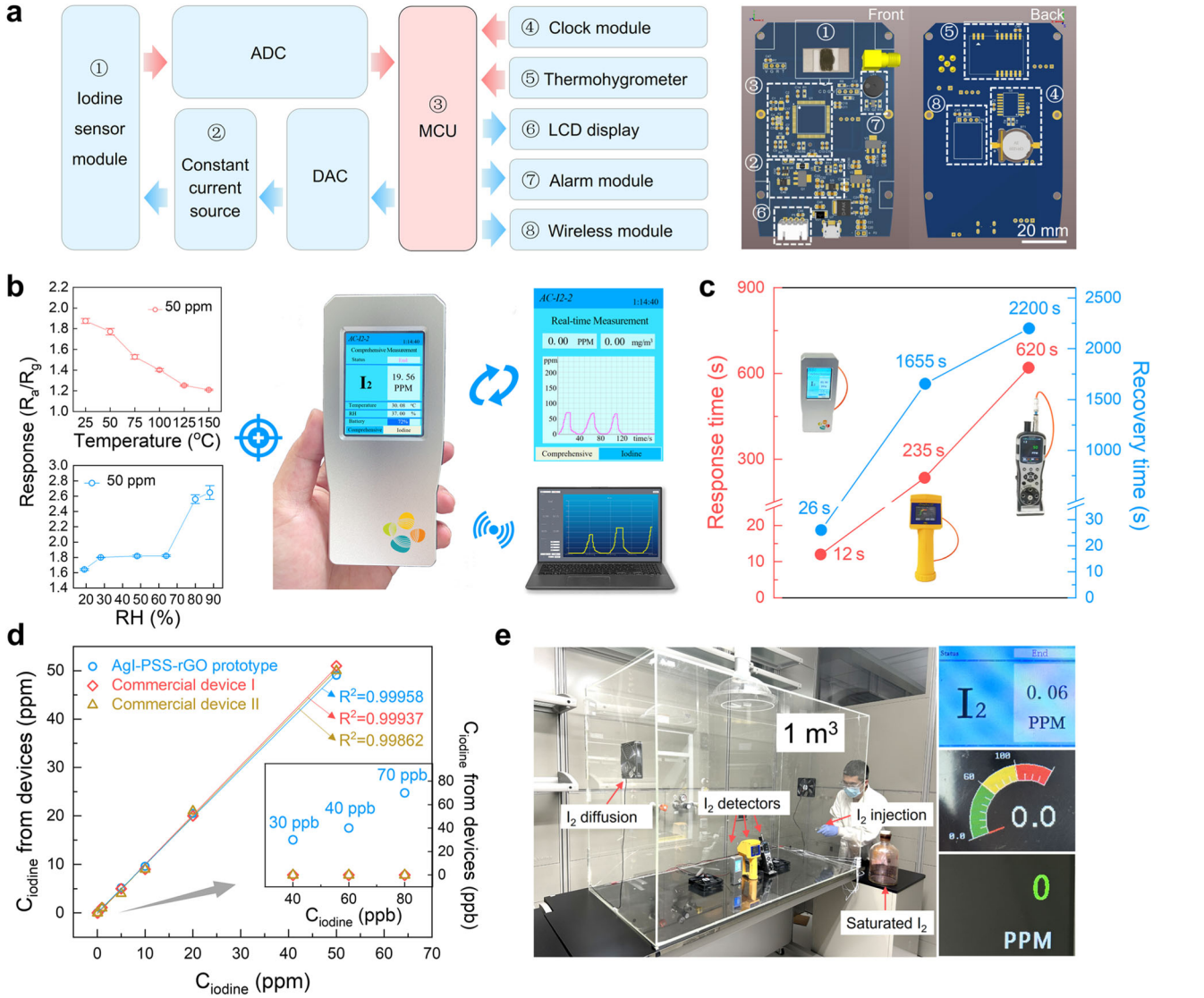

Fig. 4 | Fabrication and evaluation of an I_2 gas sensor prototype. a Operating principle and printed circuit board layout of the prototype. ADC Analog-to-Digital Converter, DAC Digital-to-Analog Converter, MCU Microcontroller Unit, LCD Liquid Crystal Display. **b** Features of the prototype, including pre-calibration for temperature and humidity effects, an adaptable user interface for comprehensive, real-time measurements, and wireless data transmission to PC terminals. **c** Comparison of response and recovery times between the prototype and two commercial I_2 gas sensors for the detection of 50 ppm I_2 gas. **d** Sensors' readouts at varying I_2 concentrations (40 ppb–50 ppm), demonstrating the prototype's capability to detect I_2 levels below 100 ppb, which commercial sensors could not achieve. **e** Photograph of the testing site and the measured I_2 concentrations displayed by the three sensors. The actual I_2 concentration in the chamber is 60 ppb, accurately detected only by our sensor. The error bars in **b** represent the standard deviations from five measurement cycles. Source data are provided as a Source Data file.

Supplementary Movie 4). Prior to testing, a quantified amount of iodine gas was injected into the chamber and left for a sufficiently long period to achieve diffusion equilibrium. The results showcased our prototype's ability to detect iodine gas in concentrations as low as tens of ppb, demonstrating superiority over commercial devices, which were ineffective below 100 ppb.

Discussion

In summary, the integration of AgI particles with rGO creates a highly effective material for detecting I_2 at low concentrations and ambient temperature. The outstanding sensing capabilities of this composite are primarily attributed to its specially designed sensing mechanism: AgI particles act as active sites for the reversible chemisorption of I_2 molecules, while the rGO offers a substantial and rapid response to the resulting polyiodides. This synergistic combination enhances the sensitivity, selectivity, and responsiveness of the detector, as confirmed by *operando* XRD and Raman spectroscopy characterizations. Furthermore, incorporating PSS into the composite significantly improves its water dispersibility and processability. This property allows for the fabrication of a highly integrated, multifunctional I_2 gas sensor prototype. When tested under identical conditions, this sensor outperformed commercial iodine gas sensors, exhibiting response and recovery times tens of times quicker, and a significantly lower detection limit, reaching levels below 100 ppb. Our study underscores the importance of innovative sensing mechanisms in the development of advanced sensors and demonstrates their practical application through the rational design of materials.

Methods

Materials and chemicals

Graphene oxide (GO, XFNANO); Poly(styrene sulfonic acid) sodium (M.W. 70,000, Alfa Aesar); Silver nitrate ($AgNO_3$, >99.8%, Sigma Aldrich); Hydrazine monohydrate (64–65%, Sigma Aldrich); Sodium hydroxide (NaOH, ≥98%, Sigma Aldrich); Ammonium hydroxide

(28–30% NH_3, Thermo Fisher Scientific). All chemicals were used as received without further purification.

Preparation of GO dispersion
GO flakes were sonicated in deionized (DI) water for 40 min to achieve a well-dispersed 1 mg/mL GO dispersion.

Preparation of rGO dispersion
4 mL of the GO dispersion (1 mg/mL) was diluted with 16 mL of DI water. Subsequently, 75 µL of ammonium hydroxide (28–30% NH_3) and 10 mL of hydrazine hydrate (0.03 mol/L) were added under mild stirring. After chemical reduction in an oil bath at 95 °C for one hour, the rGO dispersion was obtained.

Preparation of PSS-rGO dispersion
80 mg of poly(styrene sulfonic acid) sodium was dissolved in 10 mL of DI water and added to 4 mL of GO dispersion (1 mg/mL). 10 mL of hydrazine hydrate (0.03 mol/L) was added to the mixture under mild stirring. The mixture was then stirred at 80 °C for one hour in an oil bath. After cooling to room temperature, the dispersion was rinsed twice by vacuum filtration with DI water and finally re-dispersed into 20 mL DI water under mild sonication to obtain a homogeneous PSS-rGO dispersion.

Preparation of the Ag-PSS-rGO dispersion
80 mg of poly(styrene sulfonic acid) sodium was dissolved in 10 mL of DI water and added to 4 mL of GO dispersion (1 mg/mL). After that, 16 mg of $AgNO_3$, 5 mL of NaOH solution (4 mg/mL), and 10 mL of hydrazine hydrate (0.03 mol/L) were added successively to the mixture under mild stirring. The mixture was then stirred at 80 °C for one hour in an oil bath. After cooling to room temperature, the dispersion was rinsed twice by vacuum filtration with DI water and finally re-dispersed into 20 mL DI water under mild sonication to obtain a homogeneous Ag-PSS-rGO dispersion.

Fabrication of gas sensor module
To construct a blank gas sensor module, Ag-Pd interdigitated electrodes (featuring 6 pairs of digits with 200 µm fingers and 200 µm gaps) were deposited on an alumina ceramic substrate using a metal-jetting technique. The drop & dry method was then employed: 10 µL of the sensing material dispersion was applied to the IDE surface and dried on a heating holder at 60 °C for two minutes. After that, a thin sensing film formed, rendering the gas sensor module ready for measurement.

Characterizations
Atomic force microscopy was conducted on a Bruker's Dimension Icon microscope. Scanning transmission electron microscopy, selected area electron diffraction, and energy-dispersive X-ray spectroscopy were performed on a FEI Titan 80–300 microscope. X-ray photoelectron spectroscopy and X-ray diffraction were conducted on VACUTEC's Amicus XPS instrument and Bruker's D2 PHASER diffractometer, respectively.

Data availability
All data supporting the findings of this study are available within the article and the Supplementary Information file, or available from the corresponding authors on request. Source data are provided with this paper.

References

1. Barnham, K. W. J., Mazzer, M. & Clive, B. Resolving the energy crisis: nuclear or photovoltaics? *Nat. Mater.* **5**, 161–164 (2006).
2. Ewing, R. C. The Nuclear Fuel Cycle: A Role for Mineralogy and Geochemistry. *Elements* **2**, 331–334 (2006).
3. Taylor, R. *Reprocessing and Recycling of Spent Nuclear Fuel* (Elsevier, 2015).
4. Wang, H., P. Lustig, W. & Li, J. Sensing and capture of toxic and hazardous gases and vapors by metal–organic frameworks. *Chem. Soc. Rev.* **47**, 4729–4756 (2018).
5. Lebel, L. S., Dickson, R. S. & Glowa, G. A. Radioiodine in the atmosphere after the Fukushima Dai-ichi nuclear accident. *J. Environ. Radioactivity* **151**, 82–93 (2016).
6. Stohl, A. et al. Xenon-133 and caesium-137 releases into the atmosphere from the Fukushima Dai-ichi nuclear power plant: determination of the source term, atmospheric dispersion, and deposition. *Atmos. Chem. Phys.* **12**, 2313–2343 (2012).
7. Hatch, M. et al. Urinary Iodine and Goiter Prevalence in Belarus: Experience of the Belarus–American Cohort Study of Thyroid Cancer and Other Thyroid Diseases Following the Chornobyl Nuclear Accident. *Thyroid* **21**, 429–437 (2011).
8. Xia, H. & Liu, Y. Reactor Nuclear Measurements and Radiation Monitoring. In: *Measurement Science and Technology in Nuclear Engineering* (eds. Xia, H. & Liu, Y.) 315–367 (Springer Nature, 2023). https://doi.org/10.1007/978-981-99-1280-3_7.
9. Lee, U., Lee, C., Kim, M. & Kim, H. R. Analysis of the influence of nuclear facilities on environmental radiation by monitoring the highest nuclear power plant density region. *Nucl. Eng. Technol.* **51**, 1626–1632 (2019).
10. Suzuki, T., Kitamura, T., Kabuto, S., Togawa, O. & Amano, H. High Sensitivity Measurement of Iodine-129/Iodine-127 Ratio by Accelerator Mass Spectrometry. *J. Nucl. Sci. Technol.* **43**, 1431–1435 (2006).
11. Dultsev, F. N. Polymeric films based on long-chain acetylenes as sensors for iodine vapour. *Sens. Actuators B Chem.* **129**, 171–175 (2008).
12. Wang, H. Y., Ko, W. H., Batzel, D. A., Kenney, M. E. & Lando, J. B. Phthalocyanine Langmuir-Blodgett film microsensors for halogen gases. *Sens. Actuators B Chem.* **1**, 138–141 (1990).
13. Xu, M., Wang, T., Zhou, L. & Hua, D. Fluorescent conjugated mesoporous polymers with N, N -diethylpropylamine for the efficient capture and real-time detection of volatile iodine. *J. Mater. Chem. A* **8**, 1966–1974 (2020).
14. Wang, X. et al. Robust fluorescent detection of iodine vapor by a film sensor based on a polymer of intrinsic microporosity. *Chem. Eng. J.* **438**, 135641 (2022).
15. Small, L. J. & Nenoff, T. M. Direct Electrical Detection of Iodine Gas by a Novel Metal–Organic-Framework-Based Sensor. *ACS Appl. Mater. Interfaces* **9**, 44649–44655 (2017).
16. Zhou, W., Kang, C., Yu, C., Cui, Z. & Wang, X. Direct Electrical Sensing of Iodine Gas by a Covalent Organic Framework-Based Sensor. *Atmosphere* **14**, 181 (2023).
17. Small, L. J. et al. Reversible MOF-Based Sensors for the Electrical Detection of Iodine Gas. *ACS Appl. Mater. Interfaces* **11**, 27982–27988 (2019).
18. Small, L. J., Krumhansl, J. L., Rademacher, D. X. & Nenoff, T. M. Iodine detection in Ag-mordenite based sensors: Charge conduction pathway determinations. *Microporous Mesoporous Mater.* **280**, 82–87 (2019).
19. Kumar, R., Mittal, J. & Jaiswal, M. Silver coated and filled carbon nanotubes: Synthesis, electrical and thermal properties, and iodine vapor sensing. *Diam. Relat. Mater.* **120**, 108551 (2021).
20. Geim, A. K. & Novoselov, K. S. The rise of graphene. *Nat. Mater.* **6**, 183–191 (2007).
21. Lee, C., Wei, X., Kysar, J. W. & Hone, J. Measurement of the Elastic Properties and Intrinsic Strength of Monolayer Graphene. *Science* **321**, 385–388 (2008).
22. Randeniya, L. K. et al. Harnessing the Influence of Reactive Edges and Defects of Graphene Substrates for Achieving Complete Cycle of Room-Temperature Molecular Sensing. *Small* **9**, 3993–3999 (2013).

23. Robinson, J. T., Perkins, F. K., Snow, E. S., Wei, Z. & Sheehan, P. E. Reduced Graphene Oxide Molecular Sensors. *Nano Lett.* **8**, 3137–3140 (2008).
24. Feng, Q., Huang, B. & Li, X. Graphene-Based Heterostructure Composite Sensing Materials for Detection of Nitrogen-Containing Harmful Gases. *Adv. Funct. Mater.* **31**, 2104058 (2021).
25. Georgakilas, V. et al. Functionalization of Graphene: Covalent and Non-Covalent Approaches, Derivatives and Applications. *Chem. Rev.* **112**, 6156–6214 (2012).
26. Georgakilas, V. et al. Noncovalent Functionalization of Graphene and Graphene Oxide for Energy Materials, Biosensing, Catalytic, and Biomedical Applications. *Chem. Rev.* **116**, 5464–5519 (2016).
27. Yuan, W., Liu, A., Huang, L., Li, C. & Shi, G. High-Performance NO_2 Sensors Based on Chemically Modified Graphene. *Adv. Mater.* **25**, 766–771 (2013).
28. Xie, Y. et al. Ionic Functionalization of Multivariate Covalent Organic Frameworks to Achieve an Exceptionally High Iodine-Capture Capacity. *Angew. Chem. Int. Ed.* **60**, 22432–22440 (2021).
29. Xie, Y. et al. Efficient and simultaneous capture of iodine and methyl iodide achieved by a covalent organic framework. *Nat. Commun.* **13**, 2878 (2022).
30. Xie, Y. et al. Engineering the pore environment of antiparallel stacked covalent organic frameworks for capture of iodine pollutants. *Nat. Commun.* **15**, 2671 (2024).
31. Chen, J. et al. Silver-decorated ZIF-8 derived ZnO concave nanocubes for efficient photooxidation-adsorption of iodide anions: An in-depth experimental and theoretical investigation. *J. Solid State Chem.* **297**, 122039 (2021).
32. Liu, S. et al. Efficient removal of radioactive iodide ions from water by three-dimensional Ag2O–Ag/TiO2 composites under visible light irradiation. *J. Hazard. Mater.* **284**, 171–181 (2015).
33. Hanaya, M., Hatate, A. & Oguni, M. Formation of Amorphous AgI Aggregates Dominating Fast Ion Conductivity in AgI-based Glasses. *J. Therm. Anal. Calorim.* **57**, 773–785 (1999).
34. Hanaya, M., Echigo, K. & Oguni, M. Anomalous AgI composition dependence of the thermal and dielectric properties of AgI–Ag_2O–P_2O_5 glasses: evidence for the formation of amorphous AgI aggregate regions as dominating the fast Ag^+ ion conduction. *J. Phys. Condens. Matter* **17**, 2281–2292 (2005).
35. Burns, G., Dacol, F. H. & Shafer, M. W. Raman measurements of the superionic conductor AgI. *Solid State Commun.* **19**, 291–295 (1976).
36. Congeduti, A., Nardone, M. & Postorino, P. Polarized Raman spectra of a single crystal of iodine. *Chem. Phys.* **256**, 117–123 (2000).
37. Fowler, J. D. et al. Practical Chemical Sensors from Chemically Derived Graphene. *ACS Nano* **3**, 301–306 (2009).
38. Wen, Z. et al. Rhombus-shaped Co3O4 nanorod arrays for high-performance gas sensor. *Sens. Actuators B Chem.* **186**, 172–179 (2013).
39. Gao, J. et al. Amperometric gas sensors based on screen printed electrodes with porous ceramic substrates. *Sens. Actuators B Chem.* **342**, 130045 (2021).
40. Occupational Safety and Health Administration. *Permissible exposure limits–annotated tables* (United States Department of Labor. Washington, DC, 2014).
41. Barsan, M. E. NIOSH pocket guide to chemical hazards. (2007).

Acknowledgements

Y.H. acknowledges the support from the GJYC program of Guangzhou City (2024D03J0001). This work used the resources of the Supercomputing Laboratory at King Abdullah University of Science and Technology.

Author contributions

Y.H., J.T., and Z.C. conceived and designed this project. Z.C. carried out the synthesis, characterizations, and iodine gas sensing measurements. Q.L. conducted the operando characterizations. Y.M. performed the DFT calculations. J.W., J.L., G.L. and T.P., provided assistance with material characterizations. Y.Y., J.Y., and J.Z.L. supported the DFT calculations. J.S. and X.D. offered suggestions on experimental design. B.D. and Y.Z. offered guidance on the operando characterizations. Y.H. and Z.C. wrote the manuscript. All the authors discussed the results and commented on the manuscript.

Competing interests

Z.C., X.D., Y.H., and J.W. are co-inventors on an international patent 'Iodine Gas Sensor and Method' (PCT/IB2023/050847) and may benefit from the commercialization of the technologies discussed in this paper. The remaining authors declare no competing interests.

Additional information

Supplementary information The online version contains supplementary material available at https://doi.org/10.1038/s41467-025-56621-3.

Correspondence and requests for materials should be addressed to Jun Tao or Yu Han.

Peer review information *Nature Communications* thanks Keqin Deng, Jagjiwan Mittal and the other, anonymous, reviewer(s) for their contribution to the peer review of this work. A peer review file is available.